

This item is the archived peer-reviewed author-version of:

Terahertz optoelectronic properties of synthetic single crystal diamond

Reference:

Xiao Huan, Zhang Zongyan, Xu Wen, Wang Qiujing, Xiao Yiming, Ding Lan, Huang Jiangtao, Li Haowen, He Bin, Peeters François.- Terahertz optoelectronic properties of synthetic single crystal diamond
Diamond and related materials - ISSN 0925-9635 - 139(2023), 110266
Full text (Publisher's DOI): <https://doi.org/10.1016/J.DIAMOND.2023.110266>
To cite this reference: <https://hdl.handle.net/10067/2009200151162165141>

Terahertz optoelectronic properties of synthetic single crystal diamond

Huan Xiao ^{a,1}, Zongyan Zhang ^{b,1}, Wen Xu ^{c,a,d,*}, Qiuqing Wang ^a, Yiming Xiao ^{a,**}, Lan Ding ^a, Jiangtao Huang ^b, Haowen Li ^c, Bin He ^{b,***}, Francois M. Peeters ^{c,e,f}

^a School of Physics and Astronomy and Yunnan Key laboratory of Quantum Information, Yunnan University, Kunming 650091, China

^b College of New Materials and New Energies, Shenzhen Technology University, Shenzhen 515118, China

^c Micro Optical Instruments Inc., Shenzhen 518118, China

^d Key Laboratory of Materials Physics, Institute of Solid State Physics, HFIPS, Chinese Academy of Sciences, Hefei 230031, China

^e Department of Physics, University of Antwerp, Groenenborgerlaan 171, B-2020 Antwerpen, Belgium

^f Universidade Federal do Ceará, Departamento de Física, Caixa Postal 6030, 60455-760 Fortaleza, Ceará, Brazil

Highlights (85 words)

- Chemical bonds and functional groups in synthetic single crystal diamond (SCD) can result in THz optoelectronic response.
- SCD does not show typical semiconductor characteristics in THz regime. A metallic to semiconductor transition can be observed at 10 K via examining the temperature dependence of carrier density in SCD. There is a significant effect of photon-induced electronic backscattering in SCD.
- THz time-domain spectroscopy can be applied for measuring the transmittance and optical conductivity along with key electronic parameters of SCD with high resistivity.

* Corresponding author.

** Corresponding author.

*** Corresponding author.

E-mail addresses: wenxu_issp@aliyun.com (W. Xu), yiming.xiao@ynu.edu.cn (Y.M. Xiao), hebin@sztu.edu.cn (B. He)

¹ Both authors make contributions to this work.

Terahertz optoelectronic properties of synthetic single crystal diamond

Huan Xiao ^{a,1}, Zongyan Zhang ^{b,1}, Wen Xu ^{c,a,d,*}, Qiuqing Wang ^a, Yiming Xiao ^{a,**}, Lan Ding ^a, Jiangtao Huang ^b, Haowen Li ^c, Bin He ^{b,***}, Francois M. Peeters ^{c,ef}

^a School of Physics and Astronomy and Yunnan Key laboratory of Quantum Information, Yunnan University, Kunming 650091, China

^b College of New Materials and New Energies, Shenzhen Technology University, Shenzhen 515118, China

^c Micro Optical Instruments Inc., Shenzhen 518118, China

^d Key Laboratory of Materials Physics, Institute of Solid State Physics, HFIPS, Chinese Academy of Sciences, Hefei 230031, China

^e Department of Physics, University of Antwerp, Groenenborgerlaan 171, B-2020 Antwerpen, Belgium

^f Universidade Federal do Ceará, Departamento de Física, Caixa Postal 6030, 60455-760 Fortaleza, Ceará, Brazil

Abstract

A systematic investigation is undertaken for studying the optoelectronic properties of single crystal diamond (SCD) grown by microwave plasma chemical vapor deposition (MPCVD). It is indicated that, without intentional doping and surface treatment during the sample growth, the terahertz (THz) optical conduction in SCD is mainly affected by surface H-terminations, -OH-, O- and N-based functional groups. By using THz time-domain spectroscopy (TDS), we measure the transmittance, the complex dielectric constant and optical conductivity $\sigma(\omega)$ of SCD. We find that SCD does not show typical semiconductor characteristics in THz regime, where $\sigma(\omega)$ cannot be described rightly by the conventional Drude formula. Via fitting the real and imaginary parts of $\sigma(\omega)$ to the Drude-Smith formula, the ratio of the average carrier density to the effective electron mass $\gamma=n_e/m^*$, the electronic relaxation time τ and the electronic backscattering or localization factor can be determined optically.

The temperature dependence of these parameters is examined. From the temperature dependence of ρ , a metallic to semiconductor transition is observed at about $T=10$ K. The temperature dependence of τ is mainly induced by electron coupling with acoustic-phonons and there is a significant effect of photon-induced electron backscattering or localization in SCD. This work demonstrates that THz TDS is a powerful technique in studying SCD which contains H-, N- and O-based bonds and has low electron density and high dc resistivity. The results obtained from this study can benefit us to gain an in-depth understanding of SCD and may provide new guidance for the application of SCD as electronic, optical and optoelectronic materials.

Keywords: single crystal diamond, terahertz time-domain spectroscopy, optoelectronic properties

1. Introduction

The mechanical, thermal, electrical and optical properties of synthetic single crystal diamonds (SCDs) are very close to these of natural diamonds [1-3]. The SCD has been already applied as an important and practical material in the fields of optics, electronics and optoelectronics [2]. For example, i) diamond is an excellent material for optical windows covering from X-ray and UV to terahertz (THz) under low-temperature and high-pressure conditions [3]; ii) it has unique quantum properties and is capable of optical and electrical control of nitrogen vacancy color centers at room temperature [4]. This feature has been utilized for high-precision magnetic field measurement [5], biological imaging [6], quantum detection [4], etc.; iii) SCD has also been used as packaging material for semiconductor IC chips owing to its extremely high thermal conductivity [7]; iv) due to its low atomic number, diamond has a relatively large neutron scattering cross section and can be used in neutron detection [8]; and v) it is an ultra-wide bandgap semiconductor which is important for application in the area of high power and high temperature electronics and IC chips [6,9]. For the application of SCD in optical and electronic materials and devices, it is of great significance and importance to know the basic physical effects and material

parameters of diamonds. Electrical transport measurement has been commonly used for the characterization and investigation of SCD [10]. However, since SCD normally has high dc resistivity and low carrier density, some transport properties (e.g., the carrier density) cannot be measured through Hall experiment which requires the fabrication of ohmic contact electrodes on the sample [11]. The accuracy and signal-to-noise ratio of the conventional electrical measurements on SCD are difficult to be controlled technically.

On the other hand, optical measurements [12] such as photoluminescence (PL) [13,14], Raman spectroscopy [15], UV-Vis absorption spectrum [16], FTIR spectrum [17], etc., are fast, easy, non-contacting and non-damaging techniques which have been applied for studying and characterizing of SCD. In recent years, the terahertz (THz) optoelectronic technique such as THz time-domain spectroscopy (TDS) [18-20] has been applied for the investigation of SCD. Because the THz photon energy ($f=1$ THz $=4.13$ meV) is much smaller than the bandgap of diamond, THz radiation can be utilized for the investigation of free-carrier dynamics in SCD. In 2020, Amoruso et al. reported [21] the THz transmittance of diamond. By using THz TDS, Ye et al. demonstrated [22] the fingerprint absorption peaks and the dielectric response trends in 0.1-3.0 THz bandwidth in polycrystalline and monocrystalline diamond films grown by chemical vapor deposition (CVD). In 2021, Pang et al. applied femtosecond (fs) lasers to induce single crystal to amorphous phase transformation in normal grade SCD flakes and proposed that such a technique can be used for realizing the THz modulators [23]. These results indicate that THz techniques are powerful tools in the study of diamonds.

In comparison to Fourier spectroscopy, a major advantage of THz TDS technique is that it can obtain the complex optical coefficients (e.g., refractive index, dielectric constant, optical conductivity, etc.) of a sample in frequency-domain without the help of the Kramers-Kronig (K-K) transformation of the experimental data. Thus, one does not need to use empirical or semi-empirical formulas for the K-K transformation in dealing with experimental data. Therefore, the real and imaginary parts of the complex optical coefficients can be obtained directly and more accurately via

transmission or reflection measurements. This study aims to apply THz TDS to study and to measure accurately the basic optical coefficients of SCD with high dc resistivity and low electron density. We intend to determine optically the key electronic parameters of SCD and to examine the temperature dependence of these parameters. Thus, we can benefit in more understanding about SCD from the viewpoint of condensed matter physics and material applications.

2. Preparation and characterization of SCD

In this study, the microwave plasma chemical vapor deposition (MPCVD) (PLASSYS, SDR150, France) was used to grow SCD [15,24], where pure hydrogen (H_2) 5 N and methane (CH_4) 5 N were taken as the precursor gases. The plasma conditions were optimized by adjusting the input microwave power and the pressure in the chamber. During the growth of SCD, the reactor chamber pressure was set at 250 mbar and H_2 and CH_4 gas flows were kept at 190 sccm and 10 sccm, respectively. Meanwhile, the microwave power was set to be at 3500 W. No intentional doping and surface treatment were made during the growth. The sample looks colorless and transparent to daylight. The SCD wafer was then cut along the crystal orientation or cleavage plane [400] and the sample size is $8 \times 8 \times 1 \text{ mm}^3$.

In this study, the SCD samples were characterized by following methods conducted at room temperature: i) X-ray diffraction (XRD, Empyrean) was applied to examine the crystal structure and quality; ii) Raman spectroscopy was used to measure the characteristic Raman shift, where the excitation wavelengths of 532 nm (InVia, Renishaw plc) and 785 nm (Avaspec, The Netherlands) were used; iii) Fourier transform infrared (FTIR, Nicolet iS 50) spectroscopy was employed to check the C-based bonds; and iv) X-ray photoelectron spectroscopy (XPS, Escalab Xi+, China) was used to evaluate the concentrations of the major elements and the major functional groups attached to the surface of SCD.

3. THz TDS measurement

In the present study, we apply the standard THz TDS technique for transmission

measurement of the SCD [19,25]. The experimental setup of our THz TDS system is shown schematically in Fig. 1: i) the fs laser beam, generated from a Ti:sapphire regenerative amplifier laser (Coherent Inc., USA. 35 fs pulse width, 800 nm central wavelength, 1 kHz repetition rate, and about 1 mJ output power), is divided into two beams by a beam splitter as the pump and probe light sources respectively; ii) the fs pump laser beam with relatively larger radiation intensity is focused on a ZnTe crystal to generate the pulsed THz wave. The THz radiation generated by the ZnTe crystal is linearly polarized; iii) the generated THz beam is focused perpendicularly on the surface of the SCD sample; iv) through a time-delay stage, the fs probe laser beam is co-linearly incident to another ZnTe crystal along with the pump laser beam, which drives the THz detector via the electro-optical (EO) sampling using quarter-wave plate and Wollaston Prism [18]; v) the strength of the THz electric field transmitted through the SCD sample, detected by the EO sampling system, is recorded by a lock-in amplifier; and vi) the SCD sample is placed on the sample holder in a superconducting refrigerator (Oxford, UK) with two quartz windows, and the sample chamber is in vacuum. Thus, we can measure the strength of the THz electric field transmitted through the SCD sample as a function of the delay time in the temperature range of 1.5 to 300 K. Additionally, the key part of the THz TDS system is sealed and filled with nitrogen gas to prevent frost forming on the optical windows of the thermostat and the absorption of water vapor and dust to the THz wave. As a result, the signal-to-noise ratio of the measurement can be largely improved [26]. The experimental setup in this study is similar to that in our previous study of the THz optoelectronic properties of carbon nanodots [25].

In the measurement, the incident THz beam is applied perpendicularly to the surface (i.e., the [400] plane, see Fig. 2(a)) of the SCD and the THz electric field is set to be polarized linearly along the x-direction of the [400] plane of the SCD. Therefore, the results obtained from the measurements relate to the optoelectronic response along the x-direction in [400] plane of the SCD.

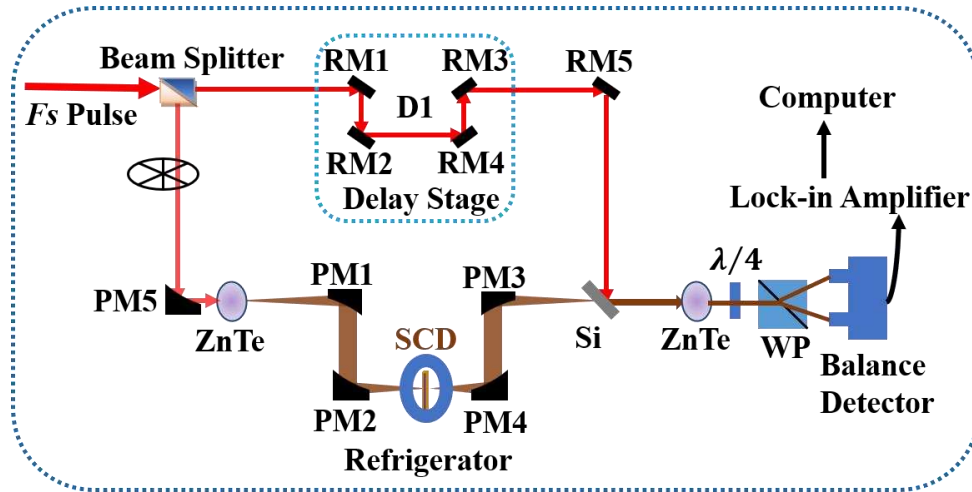


Fig. 1. Schematic diagram of the THz TDS system for transmission measurement. Here, WP, RM, and PM stand respectively for the Wollaston prism, reflection mirror, and parabolic mirror. A Si wafer is used as THz semi-transparent and semi-reflective mirror, and two ZnTe crystals are used for THz generation and detection respectively.

4. Results and discussions

4.1. Characterization of the SCD

The XRD spectrum for the SCD sample is shown in Fig. 2(a). There is a sharp peak at $2\theta=120^\circ$, which corresponds to the [400] crystal plane. This indicates that the crystal orientation of SCD originates from the [100] direction and the sample has high crystallinity. The Raman spectra are shown in Fig. 2(b). The sharp characteristic Raman peaks for SCD can be observed at 1332.5 cm^{-1} with 532 nm excitation and at 1334.42 cm^{-1} with 785 nm excitation. This peak is induced by the G-band Raman shift due to electron interaction with longitudinal optic (LO) phonons in SCD [27]. There is no characteristic peak of non-diamond carbon phases observed in the spectra, suggesting the excellent crystal quality and the purity of our SCD sample. The FTIR spectrum for SCD is shown in Fig. 2(c). It should be noted that the region from 2680 to 1600 cm^{-1} covers the major lines for intrinsic multi-phonon absorption from the C-C bonds of the SCD due to dipole momentum changes [16]. The typical diamond peak at 2158 cm^{-1} can be seen clearly.

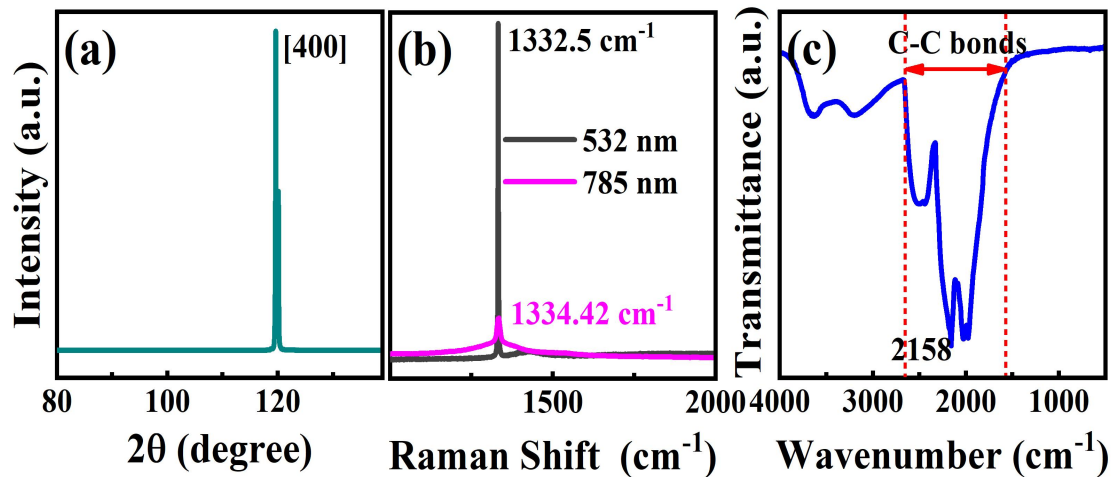


Fig. 2. (a) XRD spectrum, (b) Raman spectra excited by two wavelengths as indicated, and (c) FTIR spectrum of SCD.

Fig. 3(a) shows the full-scan XPS spectrum of the SCD. From the peaks at 284.8 eV, 399.19 eV and 532.07 eV, we learn that the SCD used in this study consists mainly of C (91.72%), N (3.57%) and O (4.69%). The high resolution XPS spectra for C 1s, N 1s and O 1s are shown in Fig. 3(b), (c) and (d), respectively. We note that: i) from Fig. 3(b), the high-resolution C 1s spectrum can be deconvoluted into three contributions from C=C (red curve), C-C (blue curve) and C=O (green curve) bonds, which are peaked at 284.46 eV, 285.01 eV and 287.45 eV, respectively; ii) the N 1s spectrum in Fig. 3(c) can be deconvoluted into two contributions peaked at 399.2 eV for pyridinic N (red curve) and at 399.65 eV for amino N (blue curve); and iii) the O 1s spectrum in Fig. 3 (d) is attributed mainly from -OH (red curve and peaked at 530.95 eV) and C=O (blue curve and peaked at 532.21 eV) based functional groups. It should be noted that the SCD sample was grown by MPCVD with taking H₂ and CH₄ as feed gases, which can normally result in the presence of hydrogen (H) terminations on the surface of SCD sample [6,28] and of -OH-based functional groups on the surface and in the body of the SCD. The conventional XPS cannot measure easily the H-bonds on the sample surface because the binding energies of C-H bonds are close to that of C=C bonds. Together with relatively large contents of N (3.57%) and O (4.69%) and the associated N- and O-based bonds and functional groups found by our

XPS measurements, we would like to point out that there are impurities and defects existing not only on the surface but also in the body of our SCD sample.

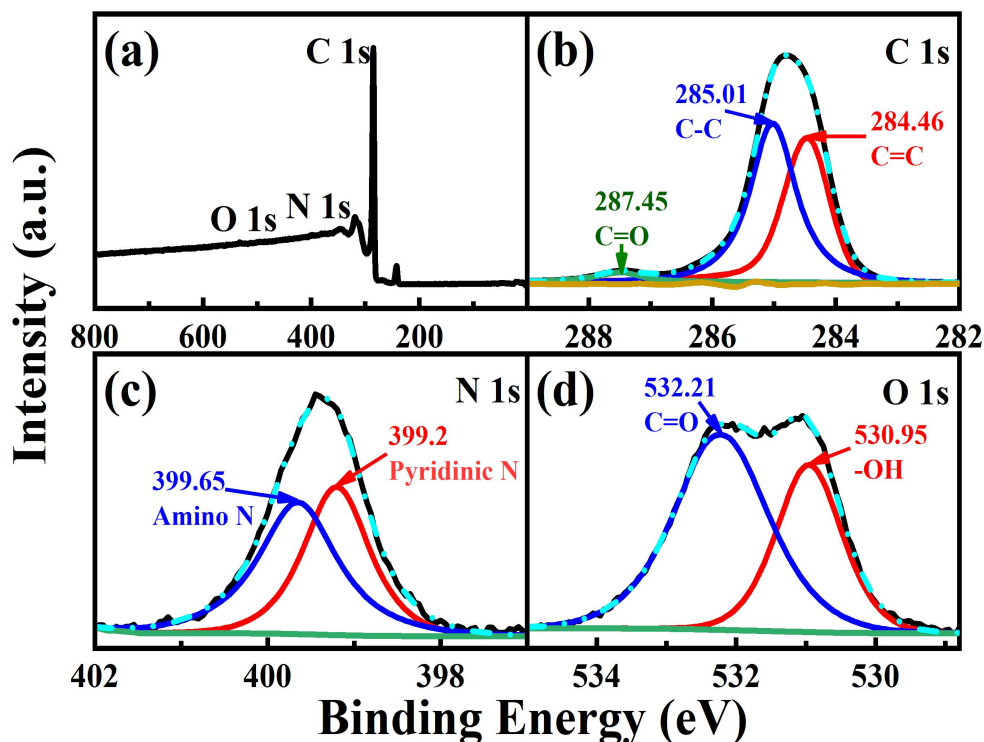


Fig. 3. (a) Full-scan XPS spectrum of SCD and the high resolution XPS spectra for C 1s (b), N 1s (c) and O 1s (d), where the contributions from different chemical bonds and functional groups are indicated.

4.2. THz transmission spectrum

The basic principle of THz TDS is to use fs laser pulse to generate and detect the time-resolved THz electric field transmitted through the sample and to obtain spectral information of the measured sample through Fourier transformation. In recent years, we have applied the THz TDS technique for the investigation of low-dimensional and nanostructured electronic systems such as graphene [29], monolayer (ML) MoS₂ [26, 30], ML WS₂ [31], ML hBN [32,33], carbon nanodots [25], etc. In the present study, we take a similar approach for studying the optoelectronic properties of SCD. Firstly, we measure the no-load THz transmission electric field in the time-domain at room temperature as reference $E_{air}(t)$. Then we measure the THz transmission electric field through the SCD sample $E_{scd}(t)$ in the time-domain (see inset in Fig. 4) at different

temperatures. The corresponding THz electric fields in the frequency-domain, $E_{scd}(\omega)$ and $E_{air}(\omega)$, can be obtained through the Fourier transformation of $E_{scd}(t)$ and $E_{air}(t)$. Fig. 4 shows the amplitude and the phase angle of $E_{scd}(\omega)$ for SCD in the frequency-domain at different temperatures. As we can see, the amplitude of $E_{scd}(\omega)$ decreases and shows a slight blue shift with increasing temperature, whereas the phase angle of $E_{scd}(\omega)$ (which is negative) depends weakly on temperature and increases almost linearly with radiation frequency.

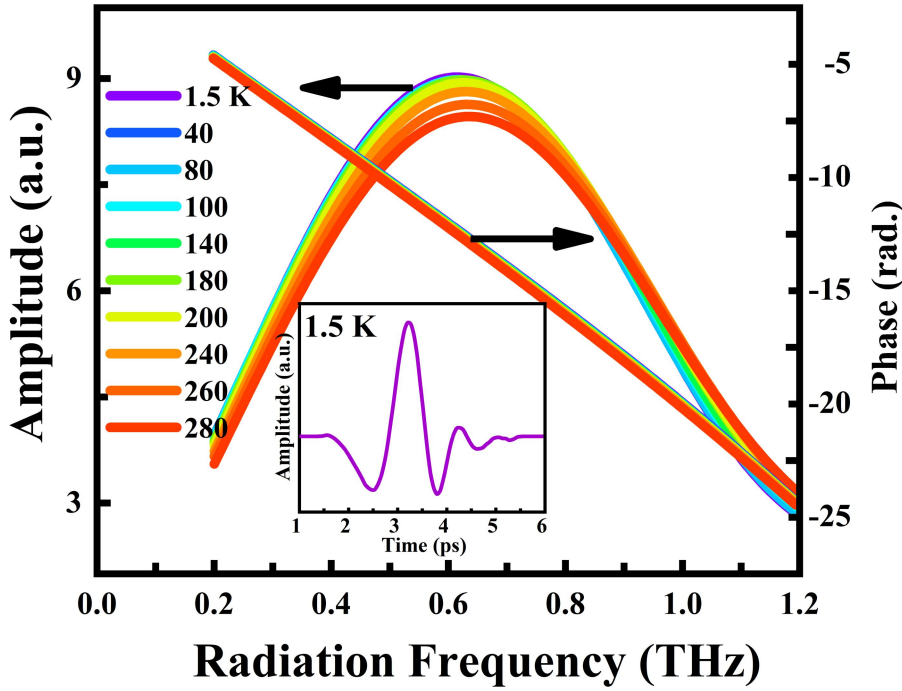


Fig. 4. Amplitude and phase angle of THz transmission electric field as a function of radiation frequency $f=\omega/2\pi$ for SCD at different temperatures as indicated. The inset shows the THz electric field transmitted through the SCD in the time-domain at a fixed temperature of 1.5 K.

From the results of $E_{scd}(\omega)$ and $E_{air}(\omega)$, we can obtain the THz transmittance, $T(\omega)$, of the SCD sample via:

$$T(\omega) \approx |E_{scd}(\omega)/E_{air}(\omega)|, \quad (1)$$

where $|E_j(\omega)|$ is the amplitude of the corresponding THz electric field strength in frequency-domain. In Fig. 5, we plot the $T(\omega)$ of SCD as a function of radiation frequency $f=\omega/2\pi$ from 0.2 THz to 1.2 THz for temperatures T from 1.5 K to 300 K.

We find that $T(\omega)$ decreases rather slowly with increasing THz radiation frequency and temperature. We note that the features of THz transmission shown in Fig. 5 are basically the same as optical window grade diamond plates grown by CVD using, e.g., Element Six BV (E6) Co., where the THz transmittance is about 70 % [34]. The decrease in $T(\omega)$ with increasing T is attributed from the fact that optical absorption increases with T . These results indicate and confirm further that SCD can be used as THz optical window material working in a wide temperature range [3].

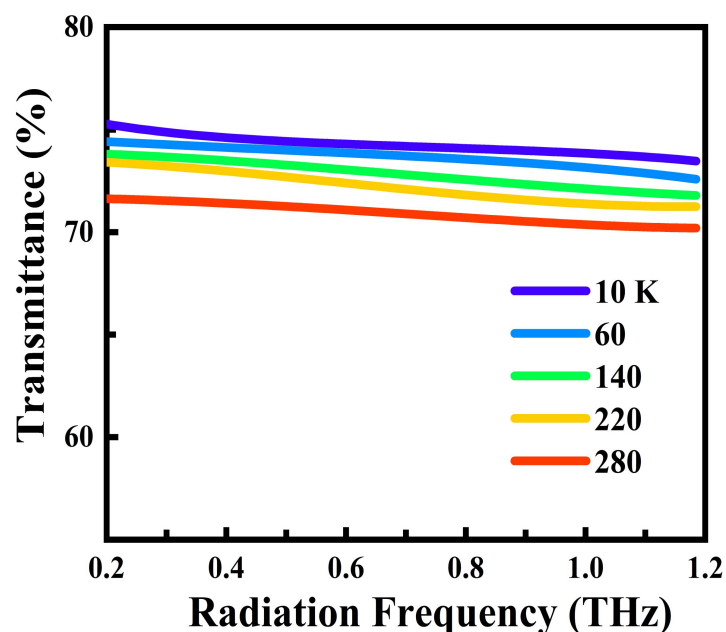


Fig. 5. THz transmission spectrum for SCD as a function of radiation frequency $f=\omega/2\pi$ at different temperatures as indicated.

4.3. Complex dielectric constant and optical conductivity

The results obtained from our sample characterization indicate that the SCD grown by using MPCVD without intentional doping and surface treatment during the growth are with H-terminations and N- and O-based chemical bonds and functional groups on the surface and in the body of SCD. The presence of these impurities and defects can result in surface and bulk conductions of the sample. The surface conduction σ_s is mainly induced by H-terminations, while the bulk conduction σ_b comes mainly from carriers induced by the activation and ionization of N- and O-based impurities and defects in diamond. Technically, it is very hard to distinguish

experimentally the contributions from σ_s and σ_b in a sample and to determine quantitatively the width region of the surface conduction. In this study, we assume an averaged or effective conduction σ attributed from surface and bulk conduction. Since the results are obtained from optical transmission through a relatively thick SCD sample, σ can be considered as a consequence of two series connected resistances via $1/\sigma=1/\sigma_s+1/\sigma_b$. Thus, we can use the bulk model and approach to deal approximately with the situation. With $E_{scd}(\omega)$ and $E_{air}(\omega)$ obtained from THz TDS measurement, we can obtain the complex refractive index $n(\omega)=n_1(\omega)+in_2(\omega)$ for SCD sample via a standard relation between the transmission coefficient and the refractive index for a bulk sample. For an air-SCD-air configuration, the transmission coefficients are [35]

$$t_{air-scd}=2/(1+n) \text{ and } t_{scd-air}=2n/(1+n). \quad (2)$$

Here t_{a-b} is the transmission coefficient for a light beam from layer a to layer b . Therefore [35],

$$\frac{E_{scd}(\omega)}{E_{air}(\omega)} = A(\omega) \exp[-i\phi(\omega)] = t_{air-scd} t_{scd-air} \exp\left[-i\omega d \frac{n(\omega)-1}{c}\right], \quad (3)$$

where $A(\omega)$ and $\phi(\omega)$ are respectively the amplitude and the phase angle of the complex transmission coefficient [note that the transmittance $T(\omega)=A^2(\omega)$], and c and d are respectively the light velocity in vacuum and the thickness of the sample. Thus, for the case of weak optical absorption $n_1(\omega) \gg n_2(\omega)$, we have

$$A(\omega) \approx \frac{4n_1(\omega)}{[n_1(\omega)+1]^2} \exp\left[-\frac{\omega d n_2(\omega)}{c}\right] \text{ and } \phi(\omega) \approx \frac{\omega d [n_1(\omega)-1]}{c}. \quad (4)$$

(4)

Using $A(\omega)$ and $\phi(\omega)$ obtained experimentally, we can determine

$$n_1(\omega) = \frac{c\phi(\omega)}{\omega d} + 1 \quad \text{and} \quad n_2(\omega) = \frac{-c \ln \left[\frac{A(\omega) [n_1(\omega)+1]^2}{4n_1(\omega)} \right]}{\omega d}. \quad (5)$$

(5)

The complex dielectric constant $\varepsilon(\omega)$ for SCD is given as

$$\varepsilon(\omega) = \varepsilon_1(\omega) + i\varepsilon_2(\omega) = n^2(\omega). \quad (6)$$

Consequently, from THz TDS measurement, we can directly measure the complex dielectric constant for a SCD sample. In Fig. 6, we show $\epsilon_1(\omega)$ and $\epsilon_2(\omega)$ as a function of radiation frequency at two temperatures $T=5$ K and 300 K. As we can see, $\epsilon_1(\omega)$ does not vary markedly with $f=\omega/2\pi$ in 0.2-1.2 THz regime, whereas $\epsilon_2(\omega)$ decreases monotonously with increasing THz radiation frequency. We note that the values of $\epsilon_1(\omega)$ measured here are very close to the static dielectric constant [36,37] for SCD at room temperature and the values of $\epsilon_2(\omega)$ are relatively small especially in high frequency regime. We also see that both $\epsilon_1(\omega)$ and $\epsilon_2(\omega)$ depend weakly on temperature.

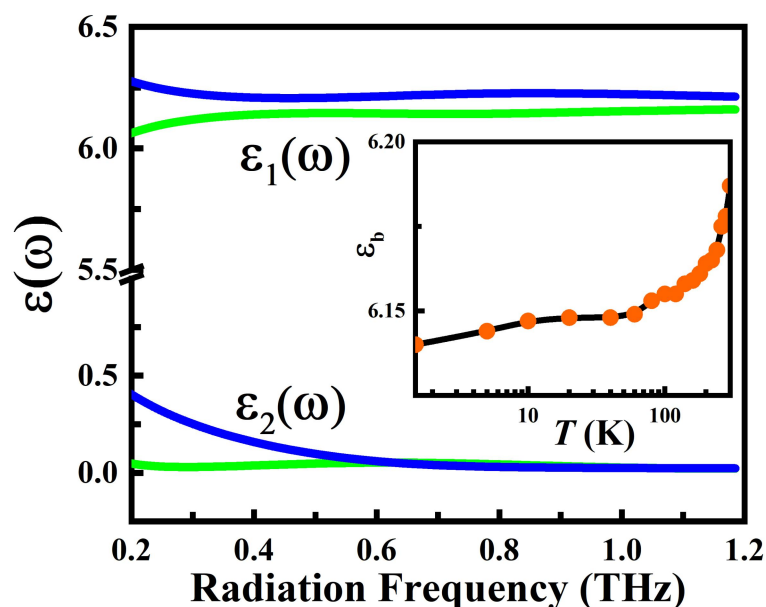


Fig. 6. Real $\epsilon_1(\omega)$ and imaginary $\epsilon_2(\omega)$ parts of complex dielectric constant for SCD as a function of radiation frequency $f=\omega/2\pi$ at 5 K (green curves) and 300 K (blue curves). The inset shows the temperature dependence of the background or static dielectric constant ϵ_b for SCD.

From a viewpoint of physics, optical conductivity is one of the most important physical quantities for an electronic system, from which one can obtain the optical coefficients such as the absorbance, refractive index, dielectric constant, etc. It is also a bridge quantity between optics and condensed matter physics. For example, the relationship between $\sigma(\omega)$ and the complex dielectric constant for an electronic material is [32]

$$\varepsilon(\omega) = \varepsilon_b + i\sigma(\omega)/(\omega\varepsilon_0) \quad \text{and} \quad \sigma(\omega) = \sigma_1(\omega) + i\sigma_2(\omega),$$

(7)

where ε_0 is the permittivity of the vacuum and ε_b is the background or static dielectric constant of the material. Using Eq. (7) and $\varepsilon(\omega)$ obtained experimentally, we can obtain ε_b (see inset in Fig. 6) and the real $\sigma_1(\omega)$ (black circles in Fig. 7) and imaginary $\sigma_2(\omega)$ (red circles in Fig. 7) parts of the optical conductivity for SCD. We find that ε_b increases slightly with temperature. It was found that $\varepsilon_1(\omega)$ for a polycrystalline diamond disk is about 5.7 – 5.75 in 10 GHz -1 THz regime [38]. The larger $\varepsilon_1(\omega)$ for SCD shown in Fig. 6 is mainly because of the larger ε_b . It is known that ε_b is mainly induced by electric dipoles in an electronic material. The presence of N- and O- based chemical bonds and functional groups in our SCD sample can increase the electric dipoles in the sample. Furthermore, the presence of the grain boundaries in polycrystalline diamond may reduce the effective electric dipoles in the sample.

Meanwhile, $\sigma_1(\omega)$ for SCD increases monotonously with f and decreases slowly with increasing temperature, whereas $\sigma_2(\omega)$ is negative in 0.2-1.2 THz regime and in 5-280 K temperature regime. These behaviors of $\sigma_1(\omega)$ and $\sigma_2(\omega)$ do not obey the conventional Drude formula for optical conductivity of an electron gas system [39,40]. The Drude formula is given as: $\sigma(\omega) = \sigma_0/(1-i\omega\tau)$, where $\sigma_0 = n_e e^2 \tau / m^*$ is the dc conductivity, n_e is the carrier density, τ is the electronic relaxation time, and m^* is the effective electron mass. It suggests that $\sigma_1(\omega)$ should decrease monotonously with increasing ω and $\sigma_2(\omega)$ should always be positive. In this study, we assume a bulk model given by Eqs. (2) and (3) to count the averaged contributions of optical conductivity from surface and bulk conducting channels. Therefore, n_e is an averaged or effective carrier density in the sample, which is with a dimension of the bulk density. Furthermore, we employ the modified Drude-Smith formula (DSF) [40,41] for the understanding of the experimental results. By taking only the first collision term in the general Drude-Smith formula into consideration, the DSF can be written as [40]:

$$\sigma(\omega) = \frac{\sigma_0}{1-i\omega\tau} \left[1 + \frac{\beta}{1-i\omega\tau} \right], \quad (8)$$

where the coefficient $\beta \in [-1, 0]$ refers to the fraction of original velocity for an electron after a collision event, which corresponds to the effect of photon-induced electronic backscattering or localization [40]. When $\beta=-1$, the carriers in the electronic system are fully back-scattered or localized and the conductivity $\sigma(\omega \rightarrow 0) = 0$. When $\beta=0$, the DSF turns into the conventional Drude formula and the carriers are in free motion [40,41]. We find that both $\sigma_1(\omega)$ and $\sigma_2(\omega)$ given by the DSF can fit very well to our experimental results, as shown in Fig. 7 (see solid curves) for temperatures from 5 K to 280 K.

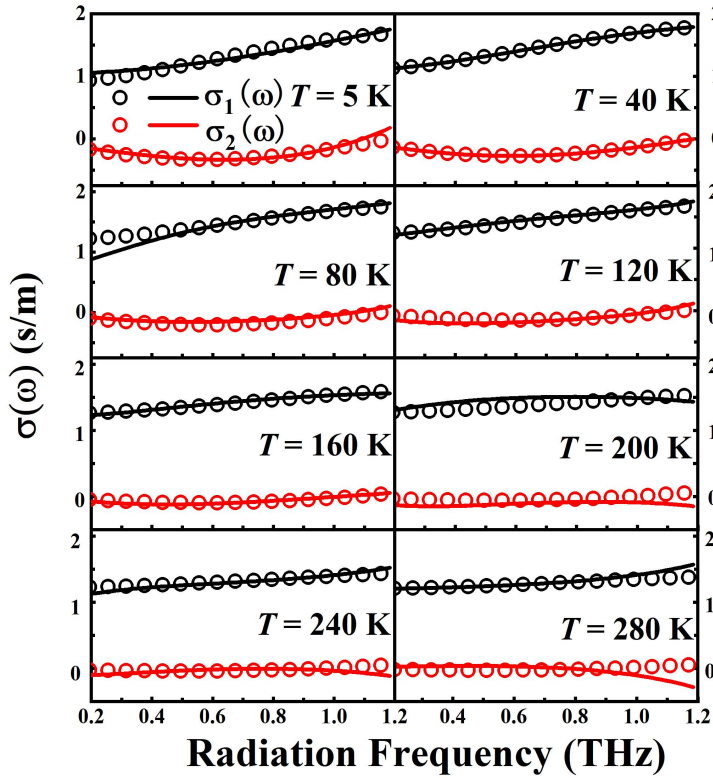


Fig. 7. Real [$\sigma_1(\omega)$, black circles and curves] and imaginary [$\sigma_2(\omega)$, red circles and curves] parts of optical conductivity for SCD as a function of radiation frequency $f=\omega/2\pi$ at different temperatures as indicated. Here the experimental and theoretical results are represented, respectively, by circles and curves.

It is known that in good metals and semiconductors, the optical conductivity induced by free carrier absorption can be described by the Drude formula. However,

in poor metals [42] and semiconductors [43] the deviations of the optical conductivity from the Drude behavior can be observed experimentally. The DSF was proposed to understand the non Drude-like optical conductivity on the basis of electronic backscattering with the inclusion of the Poisson statistics [40]. In recent years, the Drude-Smith like optical conductivity has been observed experimentally in nanostructured materials [32], two-dimensional electronic systems [32,44], carbon nanodots [25], etc. The results shown in Fig. 7 implies that the SCD does not show typical features of a good semiconductor in THz regime. This is because the conducting carriers in SCD come mainly from surface H-terminations and from those induced by the activation and ionization of -OH-, O- and N-based impurities and defects in SCD.

4.4. Key electronic parameters of SCD

Through fitting $\sigma_1(\omega)$ and $\sigma_2(\omega)$ with the DSF, we can determine the key electronic parameters of the SCD, such as the dc conductivity $\sigma_0 = n_e e^2 \tau / m^*$, the electronic relaxation time τ , and the electronic backscattering or localization factor β . Normally, the averaged carrier density in the sample can be evaluated with the obtained values of σ_0 and τ if we know the effective electron mass m^* . However, for SCD grown by MPCVD without intentional doping and surface treatment during the sample growth, low carrier density and high dc resistance are normally the case. As a result, it is very difficult technically to identify if the sample is n- or p-type through the Hall measurement. Furthermore, we know that the surface H-terminations on SCD are electro-positivity [6,28], whereas the -OH, C-O and N-based chemical bonds and functional groups in SCD are electro-negativity [45]. Because the electrons and holes in SCD are with different effective masses, we do not know which effective electron mass can be taken for evaluating the carrier density if we cannot identify the conducting type of the carriers in the sample. In this study, we take the ratio of the average carrier density to the effective electron mass $\gamma = n_e / m^*$ for examining the temperature dependence of the carrier density because m^* in SCD normally depends very weakly on temperature.

In Fig. 8(a), γ in SCD is shown as a function of temperature T . We find that

when T is less than 10 K, γ depends weakly on temperature. When T is larger than 10 K, γ increases with T and can be fitted nicely by the Arrhenius relation:

$$A = \alpha \cdot \exp(-\Delta E/k_B T),$$

(9)

where $\alpha = 1.89 \times 10^{45} \text{ cm}^{-3} \text{ kg}^{-1}$ and the activation energy is $\Delta E = 0.41 \text{ meV}$. It implies that the carriers in SCD are in metallic-like phase when $T \leq 10 \text{ K}$ and are in semiconductor-like phase when $T > 10 \text{ K}$. The metallic to semiconductor transition temperature is at about 10 K for our SCD sample. When $T > 10 \text{ K}$, the activation energy for SCD is $\Delta E = 0.41 \text{ meV}$, indicating that the thermal activation of surface H-terminations, O- and N-based chemical bonds and functional groups can be easily achieved in SCD and the γ increases exponentially with temperature from 10 K up to at least room temperature. Because H-, N- and O-based chemical bonds and functional groups are very sensitive to THz radiation field [46,47], the thermal activation of the carriers can occur more strongly in SCD in the presence of THz radiation.

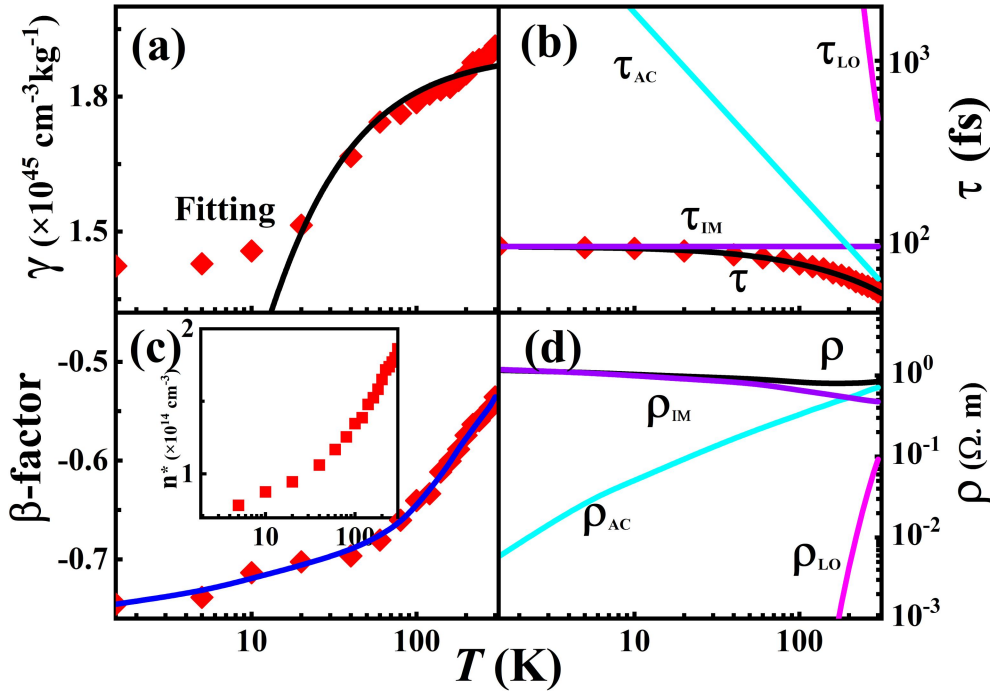


Fig. 8. (a) Ratio of the average carrier density to the effective electron mass $\gamma = n_e/m^*$, (b) electronic relaxation time τ , (c) electronic localization factor β , and (d) dc resistivity ρ as a function of temperature for SCD. In (a)-(c), the red dots are experimental results, the black curve in (a) is obtained by fitting with Eq. (9), the curves in (b) are obtained by fitting with Eq. (10) and

the contributions from different scattering mechanisms are indicated, the blue curve in (c) is drawn to guide the eye, and the inset in (c) shows the temperature dependence of the effective carrier density n^* in SCD by taking $m^*=0.23m_e$. In (d), the contributions from different scattering centers to dc resistivity of SCD are presented by using Eq. (10).

In Fig. 8(b), the temperature dependence of the electronic relaxation time τ is presented for SCD (red dots). We find that τ decreases with increasing T and can be well fitted by [48]:

$$\frac{1}{\tau} = \frac{1}{\tau_{IM}} + \alpha_{AC}T + \Gamma_{LO}N_0,$$

(10)

where τ_{IM} comes from impurity scattering and is independent on T , $1/\tau_{AC}=\alpha_{AC}T$ is attributed from acoustic-phonon scattering with α_{AC} being a fitting parameter, and $1/\tau_{LO}=\Gamma_{LO}N_0$ is the contribution from LO-phonon scattering with Γ_{LO} being a fitting parameter, $N_0=[\exp(E_{LO}/k_B T)-1]^{-1}$ the LO phonon occupation number, and E_{LO} the LO-phonon energy. For SCD, $E_{LO}=165.18$ meV [49] as is also shown from in the G-band Raman shift of SCD (see Fig. 2(b)). Through fitting, we obtain $\tau_{IM}=93.17$ fs, $\alpha_{AC}=2.702 \times 10^{10} \text{ s}^{-1}\text{K}^{-1}$ and $\Gamma_{LO}=1.24224 \times 10^{14} \text{ s}^{-1}$ for SCD. The contributions from different electronic scattering centers in SCD are shown in Fig. 8(b) as a function of temperature (curves). As we can see, the decrease in τ with increasing temperature is mainly caused by electron coupling with acoustic-phonons. This is because the impurity scattering in carbon-based materials depends very little on temperature [50] and the LO-phonon energy in diamond is very large. As a result, the temperature dependence of the electronic relaxation time in SCD is mainly determined by acoustic-phonon scattering up to room temperature [51].

In Fig. 8(c), we show the electronic localization factor β as a function of temperature. We find that the value of β decreases slowly with increasing temperature up to 60 K and it decreases sharply with increasing T in the temperature range from 60 K to 300 K, noting that β is a negative factor. This implies that the photon-induced electronic backscattering or localization weakens with increasing temperature in SCD.

By taking $\omega \rightarrow 0$ in Eq. (8), we get: $\sigma(0) = \sigma_0(1 + \beta)$. Thus, the effective conducting carrier density in the presence of electronic backscattering or localization in SCD becomes: $n^* = n_e(1 + \beta)$. To get an idea about how large the averaged conducting carrier density in our SCD sample is, we take the effective mass for an electron along the x-direction in [100] plane of diamond, $m^* = 0.23 m_e$ [52] with m_e being the rest electron mass, to evaluate n^* . The temperature dependence of n^* is shown in the inset of Fig. 8(c). Similar to γ , n^* depends weakly on T when $T \leq 10$ K and increases with T when $T > 10$ K, indicating that the metallic to semiconductor transition can also be observed by looking at the temperature dependence of the effective carrier density in SCD. Because β is a negative factor, n^* is generally less than n_e , implying the electronic localization. From inset in Fig. 8 (c), we see that when taking $m^* = 0.23 m_e$ [52], $n^* \sim 10^{14} \text{ cm}^{-3}$. If the sample is p-type, n^* should be larger because m^* for a hole is heavier. Such value is at least 10 times larger than bulk carrier density in a non-doped diamond [53]. There are two major reasons behind this higher value. First, the carrier density obtained from our THz TDS measurement is the averaged contribution from surface and bulk optical conduction, where the contribution from surface H-terminations is also included. Second, our sample is with relatively large contents of N (3.57%) and O (4.69%) and the associated N- and O-based chemical bonds and functional groups, found by our XPS measurements, implying the presence of charged impurities and defects in our sample.

By using the sample parameters obtained through fitting the experimental data with the theoretical formula, the dc resistivity $\rho = m^*/(n^* e^2 \tau)$ can be obtained for SCD in the presence of photon-induced electronic backscattering or localization effect. In Fig. 8(d), the contributions to ρ from different electronic scattering mechanisms, ρ_{IM} , ρ_{AC} and ρ_{LO} , are plotted as a function of temperature. We note that ρ in our SCD sample depends weakly on temperature from 1.5 K to 300 K. The temperature dependence of ρ for SCD looks weaker than that of γ and of τ (see Fig. 8(a) and (b)). This is because the decrease in τ is partially offset by the increase in n^* with increasing temperature. Furthermore, from dc resistivity obtained from THz TDS measurement, we can estimate the square resistance of our SCD sample, which is about $10^3 \Omega$ at

room temperature.

4.5. Further remarks

It is known that H-, O- and N-based chemical bonds and functional groups are very sensitive to THz radiation fields [47,54]. From the conditions of our sample growth and the XPS results shown in Fig. 3, we learn that there are surface H-terminations and -OH-, O- and N-based chemical bonds and functional groups presented in our SCD sample. The THz radiation can affect strongly the vibration and rotation of these bonds and functional groups. Therefore, the strong optoelectronic response to THz radiation can be observed experimentally in SCD via THz TDS measurement.

In this study, we find that there is a metallic to semiconductor transition in SCD at about 10 K, observed via examining the temperature dependence of γ (see Fig. 8(a)). Because the conducting carriers in SCD come mainly from surface H-terminations and from those induced by the activation and ionization of -OH-, O- and N-based bonds and functional groups, these defects and impurities cannot be thermally activated at low temperatures. Thus, γ or carrier density in SCD in low temperature regime does not alter with temperature and shows a metallic behavior when $T \leq 10$ K. In relatively high temperature regime, the thermal activation of surface H-terminations, -OH-, O- and N-based bonds and functional groups in SCD becomes possible and, thus, the temperature dependences of the carrier density and the dc resistivity in SCD show the typical behaviors of a semiconductor. It should be noted that in SCD at relatively high temperatures, with increasing temperature the increase in carrier density can be offset by the decrease in electronic relaxation time due to acoustic-phonon scattering. Hence, the dc resistivity can depend weakly on temperature up to room-temperature.

5. Conclusions

In this study, we have prepared the high quality synthetic single crystal diamond (SCD) by using the MPCVD technique. The THz TDS has been applied to measure

the optical coefficients of SCD, such as the transmittance, the complex dielectric constant and the complex optical conductivity. Through fitting the experimental results with theoretical formula, we have obtained optically the key electronic parameters of SCD. The temperature dependence of these sample parameters has been examined. The main conclusions drawn from this study can be summarized as follows.

We have found that there are the surface H-terminations and -OH-, O- and N-based chemical bonds and functional groups in SCD sample grown by MPCVD technique. These bonds and functional groups are the major sources of conducting carriers in SCD without intentional doping and surface treatment during the sample growth.

The transmittance of SCD depends on temperature and THz radiation frequency. However, it is above 70 % in 0.2-1.2 THz at room temperature and decreases with increasing radiation frequency and temperature. This finding confirms that SCD is a good material for THz optical window. The real and imaginary parts of dielectric constant in SCD depend weakly on temperature. $\epsilon_1(\omega)$ does not vary markedly with radiation frequency in 0.2-1.2 THz regime and is close to the static dielectric constant in SCD. However, $\epsilon_2(\omega)$ decreases monotonously with increasing THz radiation frequency. It is suggested that SCD is not a good semiconductor in THz regime. Its optical conductivity cannot be described rightly by the conventional Drude formula. However, the modified Drude-Smith model for optical conductivity in an electron gas can be employed to fit nicely the experimental results. Through fitting, we have determined optically the key electronic parameters of SCD, such as the ratio of the average carrier density to the effective electron mass, the electronic relaxation time and the electronic localization factor. We have found that there is a metallic to semiconductor transition at about $T=10$ K and the temperature dependence of electronic relaxation time is mainly induced by electron coupling with acoustic-phonons. Moreover, there is a significant effect of photon-induced electronic backscattering or localization in SCD.

In this study, we have demonstrated that THz TDS is a powerful optical tool in the investigation of SCD with high dc resistivity and low carrier density and in the

presence of H-, N- and O-based chemical bonds and functional groups. By using this advanced technique, we can measure directly and more accurately not only the complex optical coefficients but also the key electronic parameters of SCD. We hope that the findings obtained from this study can help us to gain more understanding of SCD and can provide a research basis for the application of SCD as electronic, optical and optoelectronic material.

Authorship contribution statement

Huan Xiao: THz measurement, data analysis, and manuscript draft. **Zongyan Zhang:** Sample preparation and characterization (XRD, Raman, FTIR, XPS). **Wen Xu:** Proposal and supervision of the research work, manuscript revisions. **Qiuqing Wang:** THz TDS experiment and data analysis. **Yiming Xiao:** Theoretical analysis and manuscript revisions. **Lan Ding:** Supervision of THz measurement. **Jiangtao Huang:** Sample preparation. **Haowen Li:** Data analysis. **Bin He:** Supervision of sample preparation and characterization, manuscript revisions. **Francois M. Peeters:** Suggestions and manuscript revisions. All authors have approved the final version of the manuscript.

Declaration of competing interest

The authors declare that they have no known competing financial interests or personal relationships that could have appeared to influence the work reported in this paper.

Acknowledgements

This work was supported by the National Natural Science foundation of China (NSFC) (Grants No. U2230122, U2067207, and 12004331), Shenzhen Science and Technology Program (No. KQTD20190929173954826), the University Engineering Research Center of Crystal Growth and Applications of Guangdong Province (2020GCZX005), Special Innovative Projects of Guangdong Province (2020KTSCX125), and Shenzhen Stable Supporting Program (SZWD2021015).

References

- [1] D. Das and M.S. Ramachandra Rao, N⁺-ion implantation induced enhanced conductivity in polycrystalline and single crystal diamond, *RSC Adv.* 11 (2021) 23686.
- [2] S.K. Tiwari, R. Pandey, N.N. Wang, V. Kumar, O.J. Sunday, M. Bystrzejewski, Y.Q. Zhu, and Y.K. Mishra, Progress in Diamanes and Diamanoids Nanosystems for Emerging Technologies, *Adv. Sci.* 9 (2022) 2105770.
- [3] A.H. Piracha, K. Ganesan, D.W.M. Lau, A. Stacey, L.P. McGuinness, S. Tomljenovic-Hanic, S. Praver, Scalable fabrication of high-quality, ultra-thin single crystal diamond membrane windows, *Nanoscale* 8 (2016) 6860.
- [4] P. Siyushev, M. Nesladek, E. Bourgeois, M. Gulka, J. Hruby, T. Yamamoto, M. Trupke, T. Teraji, J. Isoya, F. Jelezko, Photoelectrical imaging and coherent spin-state readout of single nitrogen-vacancycenters in diamond, *Science* 363 (2019) 728–731.
- [5] E. Bourgeois, A. Jarmola, P. Siyushev, M. Gulka, J. Hruby, F. Jelezko, D. Budker, M. Nesladek, Photoelectric detection of electron spin resonance of nitrogen-vacancy centres in diamond, *Nat. Commun.* 6 (2015) 8577.
- [6] D. Shin, B. Rezek, N. Tokuda, D. Takeuchi, H. Watanabe, T. Nakamura, T. Yamamoto, and C. E. Nebel, Photo- and electrochemical bonding of DNA to single crystalline CVD diamond, *Phys. Stat. Sol. (a)* 203 (2006) 3245–3272.
- [7] Y. Gao, N. Gao, H.D. Li, X.X. Yuan, Q.L. Wang, S.H. Cheng, J.S. Liu, Semiconductor SERS of Diamond, *Nanoscale* 10 (2008) 15788-15792.
- [8] M. Kobayashi, S. Yoshihashi, K. Ogawa, M. Isobe, S. Sangaroon, S. Kamio, Y. Fujiwara, M. Osakabe, A comprehensive evaluation of the thermal neutron detection efficiency by a single crystal CVD diamond detector with a LiF thermal neutron converter, *Fusion Eng. Des.* 179 (2022) 113117.
- [9] A.H. Piracha, P. Rath, K. Ganesan, S. Kuehn, W. HP Pernice, and S. Praver, Scalable Fabrication of Integrated Nanophotonic Circuits on Arrays of Thin Single Crystal Diamond Membrane Windows, *Nano. Lett.* 16 (2016) 3341–3347.
- [10] W. Deferme, A. Bogdan, G. Bogdan, K. Haenen, W. De Ceuninck, and M. Nesládek, Electrical transport measurements and emission properties of freestanding single crystalline CVD diamond samples, *Phys. Stat. Sol. (a)* 204 (2007) 3017–3022.
- [11] G.F. Zhang, T. Samuely, J. Kačmarčík, E.A. Ekimov, J. Li, J. Vanacken, P. Szabó, J.W. Huang, P.J. Pereira, D. Cerbu, and V.V. Moshchalkov, Bosonic Anomalies in Boron-Doped Polycrystalline Diamond, *Phys. Rev. Appl.* 6 (2016) 064011.
- [12] N. Cennamo, P.A.S. Jorge, Optical Measurements, *IEEE Instru. Meas. Mag.* 24(5) (2021) 3-4.
- [13] Y. Zhang, Y.N. Chen, Y.L. Liu, F.B. Fu, W.C. Yu, P. Jin, Z.G. Wang, Research on band-edge emission properties and mechanism of high-quality single-crystal diamond, *Carbon* 132 (2018) 651-655.
- [14] S.A. Malykhin, R.R. Ismagilov, F.T. Tuyakova, E.A. Obratsova, P.V. Fedotov, A. Ermakova, P. Siyushev, K.G. Katamadze, F. Jelezko, Y.P. Rakovich, A.N. Obratsov, Photoluminescent properties of single crystal diamond microneedles, *Opt. Mater.* 75 (2018) 49-55.
- [15] A.P. Bolshakov, V.G. Ralchenko, G.Y. Shu, B. Dai, V.Y. Yurov, E.V. Bushuev, A.A. Khomich,

- A.S. Altakhov, E.E. Ashkinazi, I.A. Antonova, A.V. Vlasov, V.V. Voronov, Y.Y. Sizov, S.K. Vartapetov, V.I. Konov, J. Zhu, Single crystal diamond growth by MPCVD at subatmospheric pressures, *Mater. Today Commun.* 25 (2020) 101635.
- [16] Y.F. Wang, W.F. Zhang, C.N. Lin, P.P. Ren, Y.J. Lu, C.X. Shan, S.F. Yu, Multiphoton Upconversion Emission from Diamond Single Crystals, *ACS Appl. Mater. Inter.* 10 (2018) 18935–18941.
- [17] T.P. Mollart, K.L. Lewis, C.S.J. Pickles, and C.J.H. Wort, Factors affecting the optical performance of CVD diamond infrared optics, *Semicond. Sci. Tech.* 18 (2003) S117–S124.
- [18] A. Rubano, S. Mou, L. Marrucci, and D. Paparo, Terahertz Hyper-Raman Time-Domain Spectroscopy, *ACS Photonics* 6 (2019) 1515–1523.
- [19] X.H. Xing, M. Liu, K. Kang, X. Ding, J.Q. Yao, L. Wu, Stability and optical tunability of flexible BST membrane observed in terahertz band, *Ceram. Int.* 48 (2022) 19006–19010.
- [20] L. Wu, Y. Fu, N.N. Xu, Q. Sheng, X. Zhang, Y.L. Yang, J.Q. Yao, D.G. Xu, X. Ding, J.N. Li, Z.Y. Wang, and W.L. Zhang, Observation of phase transitions of Ba_{0.6}Sr_{0.4}TiO₃-silicon hybrid metamaterial by THz spectra, *ACS Appl. Electron. Mater.* 2 (2020) 2449–2453.
- [21] S. Amoruso, A. Andreone, A. Bellucci, C. Koral, M. Girolami, M. Mastellone, S. Mou, S. Orlando, G.P. Papari, D. Paparo, R. Polini, A. Rubano, All-carbon THz components based on laser-treated diamond, *Carbon* 163 (2020) 197–201.
- [22] Y.T. Zheng, R. Zhang, X.D. Chen, P. Hing, J.L. Liu, J.J. Wei, J. Wang, C.M. Li, and H.T. Ye, Doomed Couple of Diamond with Terahertz Frequency: Hyperfine quality Discrimination and Complex Dielectric Responses of Diamond in the Terahertz Waveband, *ACS Appl. Electron. Mater.* 2 (2020) 1459–1469.
- [23] B.C. Lin, Q. Song, D.Q. Pang, B.W. Liu, W.P. Kong, Z.Y. Li, Y. Qin, M.L. Hu, Optical grating and THz polarizer based on normal grade single crystal diamond fast fabricated by fs laser, *Infrared Phys. Techn.* 115 (2021) 103703.
- [24] K.W. Hemawan, H.Y. Gou and R.J. Hemley, Diamond synthesis at atmospheric pressure by microwave capillary plasma chemical vapor deposition, *Appl. Phys. Lett.* 107 (2015) 181901.
- [25] D. Song, J.K. Tian, W. Xu, H. Wen, C. Wang, J. Tang, J. Zhang, M.M. Guo, Optically induced insulator-to-semiconductor transition in fluorescent carbon quantum dots measured by terahertz time-domain spectroscopy, *Carbon* 174 (2021) 741–749.
- [26] C. Wang, W. Xu, H.Y. Mei, H. Qin, X.N. Zhao, C. Zhang, H.F. Yuan, J. Zhang, Y. Xu, P. Li, and M. Li, Substrate-induced electronic localization in monolayer MoS₂ measured via terahertz spectroscopy, *Opt. Lett.* 44 (2019) 4139–4142.
- [27] S. Praver and R.J. Nemanich, Raman spectroscopy of diamond and doped diamond, *Phil. Trans. R. Soc. Lond. A* 362 (2004) 2537–2565.
- [28] L. Mosinska, P. Popielarski, K. Fabisiak, A. Dychalska, Effects of hydrogen termination of CVD diamond layers, *Opt. Mater.* 101 (2020) 109676.
- [29] H.Y. Mei, W. Xu, C. Wang, H.F. Yuan, C. Zhang, L. Ding, J. Zhang, C. Deng, Y.F. Wang and F.M. Peeters, Terahertz magneto-optical properties of bi- and tri-layer graphene, *J. Phys.: Condens. Matter.* 30 (2018) 175701.
- [30] H. Wen, W. Xu, C. Wang, D. Song, H.Y. Mei, J. Zhang, L. Ding, Magneto-optical properties of monolayer MoS₂-SiO₂/Si structure measured via terahertz time-domain spectroscopy, *Nano. Select.* 2 (2021) 90–98.
- [31] H.M. Dong, Z.H. Tao, L.L. Li, F. Huang, W. Xu, and F.M. Peeters, Substrate dependent

- terahertz response of monolayer WS₂, *Appl. Phys. Lett.* 116 (2020) 203108.
- [32] M. Bilal, W. Xu, C. Wang, H. Wen, X.N. Zhao, D. Song, L. Ding, Optoelectronic Properties of Monolayer Hexagonal Boron Nitride on Different Substrates Measured by Terahertz Time-Domain Spectroscopy, *Nanomaterials* 10 (2020) 762.
- [33] M. Bilal, W. Xu, H. Wen, X.J. Cheng, Y.M. Xiao, and L. Ding, Terahertz optical Hall effect in p-type monolayer hexagonal boron nitride on fused silica substrate, *Opt. Lett.* 46 (2021) 9.
- [34] V.V. Kubarev, Optical properties of CVD-diamond in terahertz and infrared ranges, *Nuclear Instruments and Methods in Physics Research A* 603 (2009) 22–24.
- [35] L. Duvillaret, F. Garet, J.L. Coutaz, Highly precise determination of optical constants and sample thickness in terahertz time-domain spectroscopy, *Applied Optics* 38(2) (1999) 409-415.
- [36] H.T. Ye, C. Q. Sun, H.T. Huang, P. Hing, Single semicircular response of dielectric properties of diamond films, *Thin Solid Films* 381 (2001) 52-56.
- [37] Q.F. Huang, S.F. Yoon, Rusli, Q. Zhang, J. Ahn, Dielectric properties of molybdenum-containing diamond-like carbon films deposited using electron cyclotron resonance chemical vapor deposition, *Thin Solid Films* 409 (2002) 211–219.
- [38] Jean-Michel Le Floch, R. Bara, J.G. Hartnett, M.E. Tobar, D. Mouneyrac, D. Passerieux, D. Cros, J. Krupka, P. Goy, and S. Carroopen, Electromagnetic properties of polycrystalline diamond from 35 K to room temperature and microwave to terahertz frequencies, *J. Appl. Phys.* 109 (2011) 094103.
- [39] H. Němec, P. Kužel, and V. Sundström, Far-infrared response of free charge carriers localized in semiconductor nanoparticles, *Phys. Rev. B* 79 (2009) 115309.
- [40] N.V. Smith, Classical generalization of the Drude formula for the optical conductivity, *Phys. Rev. B Condens. Matter.* 64 (2001) 155106.
- [41] T.L. Cocker, D. Baillie, M. Buruma, L.V. Titova, R.D. Sydora, F. Marsiglio, F.A. Hegmann, Microscopic origin of the Drude-Smith model, *Phys. Rev. B* 96 (2017) 205439.
- [42] D. Wang, Generalized Drude model and electromagnetic screening in metals and superconductors, *Chin. Phys. B* 27 (2018) 057401.
- [43] C.Y. Tsai, C.Y. Tsai, C.H. Chen, T.L. Sung, T.Y. Wu, and F.P. Shih, Theoretical Model for Intravalley and Intervalley Free-Carrier Absorption in Semiconductor Lasers: Beyond the Classical Drude Model, *Ieee J. Quantum Elect.* 34 (1998) 3.
- [44] K. Wolff, R. Schäfer, M. Meffert, D. Gerthsen, R. Schneider, and D. Fuchs, Anisotropic electronic transport of the two-dimensional electron system in Al₂O₃/SrTiO₃ heterostructures, *Phys. Rev. B* 95 (2017) 245132.
- [45] T. Sharda, A.K. Sikder, D.S. Misra, A.T. Collins, S. Bhargava, H.D. Bist, P. Veluchamy, H. Minoura, D. Kabiraj, D.K. Awasthi, P. Selvam, Studies of defects and impurities in diamond thin films, *Diam. Relat. Mater.* 7 (1998) 250-254.
- [46] H. Wang, S. Tsuchikawa, T. Inagaki, Terahertz time-domain spectroscopy as a novel tool for crystallographic analysis in cellulose: the potentiality of being a new standard for evaluating crystallinity, *Cellulose* 28 (2021) 5293–5304.
- [47] M. Takahashi, Terahertz Vibrations and Hydrogen-Bonded Networks in Crystals, *Crystals* 4 (2014) 74-103.
- [48] W. Xu, F.M. Peeters, T.C. Lu, Dependence of resistivity on electron density and temperature in graphene, *Phys. Rev. B Condens. Matter.* 79 (2009) 48-51.

- [49] J. Kulda, H. Kainzmaier, D. Strauch, B. Dorner, M. Lorenzen, and M. Krisch, Overbending of the longitudinal optical phonon branch in diamond as evidenced by inelastic neutron and x-ray scattering, *Phys. Rev. B* 66 (2002) 241202.
- [50] W. Kiciński, S. Dyjak, Transition metal impurities in carbon-based materials: Pitfalls, artifacts and deleterious effects, *Carbon* 168 (2020) 748-845.
- [51] W. Walukiewicz, Acoustic-phonon scattering in modulation-oped heterostructures, *Phys. Rev. B* 37 (1988) 8530.
- [52] H. Löfås, A. Grigoriev, J. Isberg, and R. Ahuja, Effective masses and electronic structure of diamond including electron correlation effects in first principles calculations using the GW-approximation, *Aip Adv.* 1 (2011) 032139.
- [53] T. Ichii, Y. Hazama, N. Naka, and K. Tanaka, Study of detailed balance between excitons and free carriers in diamond using broadband terahertz time-domain spectroscopy, *Appl. Phys. Lett.* 116 (2020) 231102.
- [54] Q.C. Liu, Q. Zhang, G.L. Li, Z.C. Guo, X.Y. He, C. Xie, H. Deng and L.P. Shang, Terahertz spectral investigation of temperature induced polymorphic transformation of 2,2 dinitroethylene-1,1-diamine, *RSC Adv.* 11 (2021) 6247.